

Cite this: *Nanoscale*, 2025, **17**, 7760


Received 25th November 2024,

Accepted 24th February 2025

DOI: 10.1039/d4nr04944f

rsc.li/nanoscale

H₂O₂ self-supplying nanoparticles for chemodynamic and synergistic photodynamic therapy to augment cGAS/STING activation†

 Ai-Hong Zhang,^a Wei-Chuang Kong,^a Xiao-Lei Zhang,^a Ya-Li Meng,^a Zhen-Hui Xin,^a
 Xiao-Juan Jia,^b Xu-Ying Liu^{*a} and Yan-Fei Kang  ^{*a}

Triple negative breast cancer (TNBC) characterized by easy metastasis and poor prognosis is one of the most intractable malignancies. Immunotherapy, as one of the most promising treatments for TNBC, has limited efficacy due to the immunosuppressive tumor microenvironment (ITME). Herein, copper peroxide nanodots (CPN) and chlorin e6 (Ce6) were encapsulated in a liposome with the cinnamaldehyde dimer (CDC) to improve the ITME and enhance anti-tumor activity. To be specific, after endocytosis by cancer cells, Ce6-CPN@CDC released H₂O₂ and Cu²⁺ in the acidic tumor environment. Next, Cu²⁺ was reduced by GSH to Cu⁺, and Cu⁺ catalyzed H₂O₂ to produce ·OH for chemodynamic therapy (CDT). Meanwhile, under near-infrared laser irradiation, singlet oxygen (¹O₂) can be generated from the released Ce6, exerting a robust photodynamic anticancer effect. In addition, the high ROS-induced ICD and direct DNA damage activated the cGAS-STING pathway, which significantly improved the ITME to amplify the immunostimulatory effect. *In vitro* and *in vivo* studies showed that the Ce6-CPN@CDC nanoparticle could realize effective tumor inhibition with minimal toxic side effects. Together, Ce6-CPN@CDC provides a paradigm for combining PDT and CDT to activate immunotherapy and provides a new strategy to improve the efficacy of multimodal synergistic therapy for TNBC.

1. Introduction

Cancer immunotherapy seeks to stimulate the host immune system to search for and kill tumor cells,^{1,2} and some patients with triple negative breast cancer (TNBC) have already benefited.³ Although tremendous advances have been achieved in

tumor immunotherapy, it is greatly limited by the immunosuppressive tumor microenvironment (ITME).⁴ Therefore, it is promising to enhance anti-tumor immune treatment efficiency *via* improving the ITME.^{5–8} The cyclic guanosine monophosphate adenosine monophosphate synthase (cGAS)–stimulator of interferon gene (STING) signaling pathway has emerged as a promising target for cancer immunotherapy, attributed to the fact that abnormal DNA detection through the STING pathway can trigger a robust immune response against tumors.^{9–12} When the cGAS-STING signaling pathway is activated in tumor cells, the ITME tends to be regulated and reverts to an active ‘hot’ tumor, which is advantageous for addressing the immune evasion mechanisms developed by tumors.^{13–15} Moreover, the immunogenic cell death (ICD) effect and cGAS-STING immune pathways could promote dendritic cell (DC) maturation and antigen-specific T cell infiltration. Therefore, the simultaneous activation of the cGAS-STING immune pathway and ICD may improve the anti-tumor immunotherapy effect.

ICD induced by traditional therapies (like photodynamic therapy (PDT) and chemodynamic therapy (CDT)) has become a promising approach for transforming low-immunogenic ‘cold tumors’ into ‘hot tumors’ in tumor immunotherapy.^{16–19} PDT has been widely studied as a non-invasive treatment modality for local tumor therapy, due to its notable advantages such as spatiotemporal control and low toxicity.^{20,21} Under near-infrared (NIR) light irradiation, photosensitizers (PSs) rapidly produce cytotoxic reactive oxygen species (ROS) and kill tumor cells.^{22,23} Unfortunately, owing to the shallow penetration of light through tissues, deep tumors are difficult to destroy.²⁴ Moreover, most PSs are highly dependent on oxygen to produce ¹O₂, while the lack of adequate oxygen supply (hypoxia) in solid tumors results in inefficient ROS production, leading to reduced anticancer efficacy of PDT.²⁵ Therefore, it is essential to develop hypoxia-irrelevant ROS-generating strategies.

Chemodynamic therapy (CDT), as one of the reactive oxygen species (ROS)-based therapeutics, has been recognized as an efficient anti-tumor strategy, due to its favorable anti-

^aCollege of Laboratory Medicine, Institute of Pathogen Biology and Immunology, Hebei Key Laboratory of Neuropharmacology, Hebei Key Laboratory of Quality & Safety Analysis-Testing for Agro-Products and Food and Zhangjiakou Key Laboratory of Organic Light Functional Materials, Hebei North University, Zhangjiakou, 075000 Hebei Province, China. E-mail: liuxuying0045@163.com, kangyanfei172@163.com

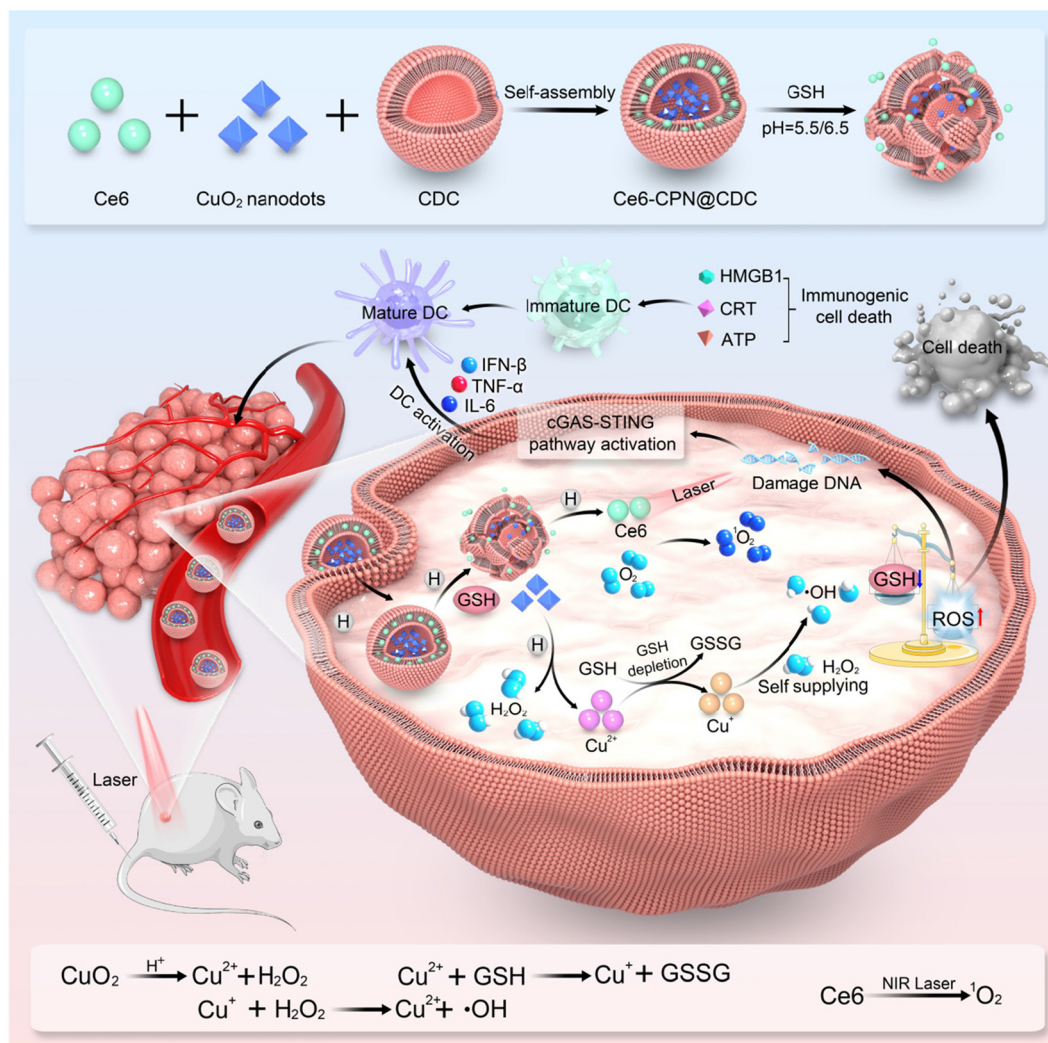
^bCAS Key Laboratory of Pathogenic Microbiology and Immunology, Institute of Microbiology, Chinese Academy of Sciences, Beijing 100101, China

†Electronic supplementary information (ESI) available. See DOI: <https://doi.org/10.1039/d4nr04944f>

tumor efficacy.²⁶ The intracellular Fenton reaction can utilize excessive H_2O_2 in cancer cells to produce highly toxic $\cdot\text{OH}$, thereby addressing the issue of inefficient ROS generation associated with PDT.^{27–29} Compared to PDT, the characteristic of reliance on oxygen is avoided in CDT.³⁰ Thus, combining PDT and CDT could potentially improve therapeutic performance. For example, Fu and coworkers reported a composite nano-assembly to significantly inhibit tumor growth. To be specific, natural small molecules (NSMs) worked together with Ce6 to provide effective CDT and PDT.³¹ Li and coworkers discovered that the multimodal combination of $\text{Fe}_3\text{O}_4\text{-CDs@Fc}$ (CDT/PDT) strongly induces immune cell death (ICD).³² Despite these advances, the role of ICD induction and cGAS-STING pathway activation by PDT and CDT has been rarely reported. We therefore hypothesized that a combination of PDT and CDT may be favorable for enhanced immunotherapeutic effects, but this hypothesis requires further validation.

Based on the above-discussed issues, the cinnamaldehyde dimer (CDC) with a lipid bilayer structure was designed to load

the photosensitizer chlorin e6 (Ce6) and copper peroxide nanodots (CPN), forming the final Ce6-CPN@CDC nanoparticle. After endocytosis by cancer cells, due to the characteristics of overexpression of GSH and slight acidity in the tumor microenvironment, the nanoparticles can undergo degradation, releasing Ce6 and CPN to exert their respective anti-tumor effects (Scheme 1). Photodynamic therapy mediated by the photosensitizer Ce6 can suppress tumor cells and trigger an immune response. However, CPN can serve as a self-supplied Fenton agent, which can be specifically triggered by the acidic tumor environment to generate a large amount of Cu^{2+} and H_2O_2 , overcoming the limited concentration of H_2O_2 in the tumor microenvironment. Moreover, PDT and CDT can cause DNA damage and enhance the activation of ICD and the cGAS-STING pathway, thereby improving the ITME to amplify the immunostimulatory effect. This promising strategy of combining PDT and CDT to activate immunotherapy could improve the therapeutic effect against TNBC and provide a new pathway for multi-synergistic tumor therapy.



Scheme 1 Formation process of Ce6-CPN@CDC NPs and the mechanism of synergistic self-enhancing CDT, PDT and immunotherapy.

2. Experimental

2.1 Synthesis of Ce6@CDC and Ce6-CPN@CDC

First, CDC (3 mg) was added to ethyl alcohol (100 μL) for use. Then, Ce6 solution (dissolved in methyl alcohol, 50 $\mu\text{g mL}^{-1}$) was added to the CPN solution (2 mL). This mixture was slowly added dropwise to the CDC solution (100 μL) and stirred at room temperature. Finally, the samples were obtained by centrifugation and washed three times at 10 000 rpm for 30 min. Under the same conditions, Ce6@CDC nanoparticles could also be obtained.

2.2 Cellular uptake

The uptake of Ce6-CPN@CDC by MDA-MB-231 cells was evaluated as follows: MDA-MB-231 cells were uniformly inoculated in a laser confocal Petri dish and cultured in a 37 °C cell culture incubator for 24 h. The medium was then replaced with a 1 mL new medium containing Ce6-CPN@CDC. After incubation for 1 h, 2 h and 4 h, the original medium was discarded and the cells were fixed with 4% paraformaldehyde. Hoechst 33342 was added to each Petri dish and stained for 5 min. The uptake of Ce6-CPN@CDC by MDA-MB-231 cells was observed by confocal laser microscopy (CLSM).

2.3 Cytotoxicity evaluation

The cytotoxicity was determined by the MTT assay. MDA-MB-231 cells were seeded at a density of 8×10^3 cells per well in a 96-well plate for 24 h. The concentration gradient of Ce6-CPN@CDC was diluted to 0.5 $\mu\text{g mL}^{-1}$, 0.75 $\mu\text{g mL}^{-1}$, 1 $\mu\text{g mL}^{-1}$, 1.5 $\mu\text{g mL}^{-1}$, 2 $\mu\text{g mL}^{-1}$, and 2.5 $\mu\text{g mL}^{-1}$ in fresh complete medium. Next, the cells were either irradiated with a 660 nm laser (60 mW cm^{-2}) for 10 min or left untreated. MTT was added to the 96-well plate and incubated for 4 h. The absorbance of the wells at 570 nm was recorded using a microplate reader. Under the same conditions, the cell survival rate of Ce6@CDC was measured. Cell viability was calculated from eqn (1):

$$\text{Cell viability (\%)} = \frac{\text{OD (test)} - \text{OD (blank)}}{\text{OD (control)} - \text{OD (blank)}} \times 100\% \quad (1)$$

2.4 Immunofluorescence analysis of γH2AX

MDA-MB-231 cells were uniformly inoculated in a laser confocal Petri dish and cultured in a 37 °C cell culture incubator for 24 h. The cells were incubated in 1 mL of fresh medium containing Ce6-CPN@CDC and Ce6@CDC. After the cells were fixed with 4% paraformaldehyde, they were permeabilized with 0.3% TritonX-100 for 10 min. The cells were incubated with the anti- γH2AX antibody overnight at 4 °C, and then Cy3-labeled secondary antibody working solution was added to the samples and incubated at 37 °C for 1 h. Subsequently, nuclei were stained with Hoechst 33342 for 5 min. Immunofluorescence images were acquired by CLSM.

2.5 *In vivo* antitumor study

All animal procedures were conducted in accordance with the "Guidelines for the Management and Use of Laboratory

Animals at Hebei North University" (SYXK (Su) 2023-015) and were approved by the Animal Ethics Committee of Hebei North University. This ensures that animal welfare and ethical standards are strictly adhered to throughout the experimental process. The audit number is HBNU20240522131. Female BALB/c mice (6 week old, 18–20 g each) were purchased from Sibeifu (Beijing) Biotechnology Co., Ltd. They were inoculated with 4T1 tumors in the right gluteal region. When the tumor volumes reached 50 mm^3 , the mice were divided into 5 groups ($n = 3$) and injected with PBS, Ce6@CDC with or without laser irradiation, and Ce6-CPN@CDC with or without laser irradiation *via* the tail vein every 2 days. Throughout the treatment period, both the body weight and tumor volume of the mice were recorded and calculated using the following formula: tumor volume (mm^3) = (length \times width²)/2. The mice were euthanized after 14 days, tumors and major organs were collected for hematoxylin and eosin (H&E) staining, and serum was obtained for ELISA.

2.6 Statistical analysis

All experimental data are presented as mean \pm standard deviation, and one-way ANOVA was used to analyze the significance between several groups (* $P < 0.05$, significant; ** $P < 0.01$, moderately significant; and *** $P < 0.001$, highly significant).

3. Results and discussion

3.1 Characterization of CPN and Ce6-CPN@CDC

Firstly, CPN was synthesized using a simple peroxidation reaction. Transmission electron microscopy (TEM) images showed that the prepared CPN had a small size of about 5–10 nm (Fig. S1, ESI†). Then, nanoparticles were prepared using a simple self-assembly method, with hydrophilic CPN in the lumen and hydrophobic Ce6 in the lipid bilayer wall, respectively (denoted as Ce6-CPN@CDC).³³ The TEM image of Ce6-CPN@CDC showed that it was spherical with a size of 120 nm (Fig. S2, ESI†), indicating the preferential accumulation of nanoparticles in tumor tissues through the enhanced permeability and retention (EPR) effect. However, the DLS measurement of Ce6-CPN@CDC showed a size of 145 nm and an obvious Tyndall effect (Fig. 1a), which was consistent with the TEM result. To determine the chemical composition of the nanoparticles, UV-Vis spectroscopy and fluorescence spectra were analyzed. It can be seen that Ce6 characteristic peaks appeared in Ce6-CPN@CDC at approximately 411 nm and 666 nm (Fig. 1b), and the fluorescence emission spectrum of Ce6-CPN@CDC was similar to that of free Ce6 (Fig. 1c), indicating the successful loading of Ce6 onto CDC. Moreover, potassium permanganate (KMnO_4) solution changed from pink to colorless when CPN or Ce6-CPN@CDC was added (Fig. 1d), demonstrating that CPN was encapsulated into CDC and H_2O_2 was generated. In addition, the characteristic peaks of CPN and Ce6 were observed in the FTIR spectra of Ce6-CPN@CDC, which further proved the formation of Ce6-CPN@CDC (Fig. 1e). Moreover, zeta-potential measurements under

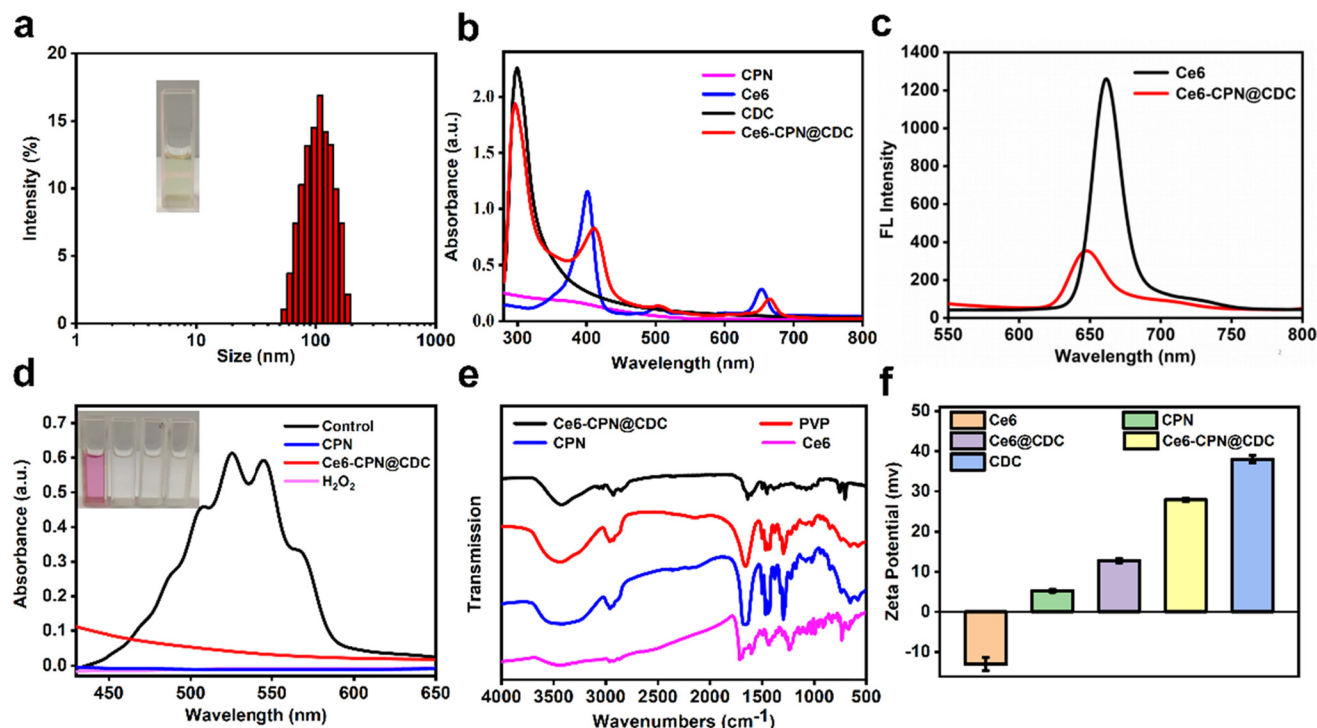


Fig. 1 (a) Hydrodynamic diameter distribution of Ce6-CPN@CDC. Inset: photograph of Ce6-CPN@CDC dispersed in water. (b) UV-Vis spectra of CPN, CDC, Ce6 and Ce6-CPN@CDC. (c) Fluorescence spectra of free Ce6 and Ce6-CPN@CDC. (d) KMnO_4 colorimetric test. Inset image shows respectively the control (only KMnO_4), CPN, Ce6-CPN@CDC and H_2O_2 from left to right. (e) FTIR spectra of Ce6-CPN@CDC, PVP, CPN and Ce6. (f) Variations in the zeta potential of Ce6, CPN, Ce6@CDC, Ce6-CPN@CDC and CDC in water.

dynamic light scattering were performed to monitor the preparation of Ce6-CPN@CDC. The zeta potential of Ce6@CDC (12.8 mV) is higher than that of Ce6 (−13 mV), making it easier for CDC-loaded Ce6 to permeate the cell through the negatively charged cell membrane.³⁴ After embedding copper peroxide with positive potential, the surface potential of Ce6-CPN@CDC increased to 27.9 mV, confirming the effective loading of CPN (Fig. 1f).

Furthermore, the stability of the nanoparticles was evaluated by measuring the change in absorbance in neutral water and DMEM medium containing 10% FBS. The absorbance value of Ce6-CPN@CDC did not change significantly within 24 h, indicating that Ce6-CPN@CDC had good biological stability and the potential to achieve long-term blood circulation *in vivo* (Fig. S3, ESI†). All these data proved the successful preliminary synthesis of Ce6-CPN@CDC and provided a basis for further experiments.

3.2 Assessment of the ROS generation ability

Adequate H_2O_2 self-supply in CPN provided a solid foundation for achieving an enhanced CDT effect. The generation of $\cdot\text{OH}$ was detected using the 3,3',5,5'-tetramethylbenzidine (TMB) indicator, as TMB could be oxidized by $\cdot\text{OH}$ to produce a blue color with characteristic absorption at 654 nm. To evaluate the $\cdot\text{OH}$ generation ability of CPN, the nanoparticles were incubated at different pH levels. The results showed that CPN caused a distinct color change in TMB at pH 5.5 within

120 min (Fig. S4a, ESI†). Additionally, the absorption peak at 654 nm increased with the extension of reaction time (Fig. S4b, ESI†), indicating that the formation of $\cdot\text{OH}$ was time-dependent. Since CPN decomposes into Cu^{2+} and H_2O_2 under acidic conditions, Ce6-CPN@CDC was an acid-induced $\cdot\text{OH}$ generator. As expected, Ce6-CPN@CDC also exhibited Fenton-like catalytic activity similar to CPN under acidic conditions (Fig. 2a) and the absorbance of TMB solution containing Ce6-CPN@CDC was time-dependent (Fig. 2b). All these results showed that Ce6-CPN@CDC could simultaneously release Cu^{2+} and H_2O_2 in an acidic microenvironment, which was expected to facilitate cancer therapy *via* CDT through a H_2O_2 self-supplying Fenton-like reaction.

In addition, the PDT activity of Ce6-CPN@CDC in an acidic environment under light irradiation was also investigated. To evaluate the $^1\text{O}_2$ generation capacity of PDT, 9,10-anthracenyl-bis(methylene) dimalonic acid (ABDA) was chosen as an indicator. As shown in Fig. 2c–e, there was minimal change at pH 7.4, while the absorbance values showed a time-dependent decrease under pH 5.5 and GSH conditions, indicating that Ce6 could be released from the nanoparticles under acidic and GSH conditions and generate singlet oxygen under light irradiation, attributed to the fact that CDC contained Schiff bases as acid-cleavable groups and alkenes as Michael addition reaction sites. Moreover, the normalization of singlet oxygen generation under three different conditions further supported the aforementioned results (Fig. 2f). All of these

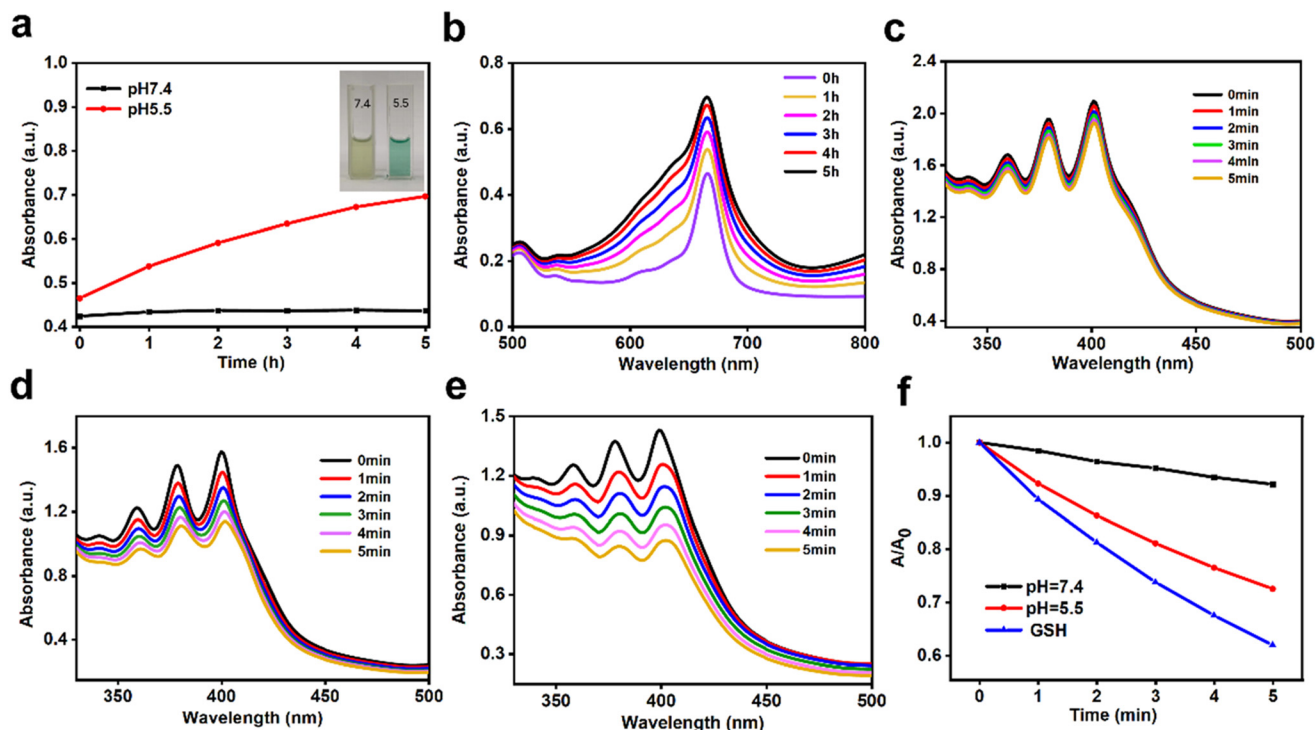


Fig. 2 (a) Time-dependent absorbance of TMB solutions with Ce6-CPN@CDC under different pH conditions. (b) Time-dependent $\cdot\text{OH}$ level with Ce6-CPN@CDC under acidic conditions. (c–e) Ce6-CPN@CDC under the 660 nm laser (60 mW cm^{-2}) generated $^1\text{O}_2$, which then reacted with ABDA. Finally, the OD value of ABDA was measured with time under different conditions (pH = 7.4, pH = 5.5, and GSH). (f) Relative UV-Vis absorbance of ABDA as a function of time after different treatments, where A_0 and A are the absorbance of ABDA at 405 nm before and after laser irradiation.

findings indicated that the Ce6-CPN@CDC nanoparticles could effectively induce PDT effects under acidic and GSH conditions.

Glutathione (GSH), an essential intracellular antioxidant, protects tumor cells from ROS-induced oxidative damage. The introduction of a GSH scavenger into tumor cells during ROS-based therapy has been shown to enhance the overall anti-tumor efficiency. Hence, we here explored the GSH elimination ability of CPN using DTNB based on the fact that colorless DTNB is reduced by GSH to form a yellow product with a distinct absorption peak at 412 nm. As illustrated in Fig. S5a and b, ESI† the absorbance intensity at 412 nm gradually decreased with decreasing pH values and was time-dependent, confirming the depletion of GSH by CPN in an acidic environment. Meanwhile, Ce6-CPN@CDC also reduced the GSH level over time, indicating that ROS-based therapy *via* Ce6-CPN@CDC was improved by GSH consumption (Fig. S5c, ESI†).

3.3 Intracellular ROS detection

The Ce6-CPN@CDC-mediated ROS generation, including $^1\text{O}_2$ and $\cdot\text{OH}$, in MDA-MB-231 cells was studied using the ROS probe, 2,7-dichlorofluorescein diacetate (DCFH-DA), which undergoes oxidation to produce fluorescent DCF (Fig. 3a). It was observed that the fluorescence changed negligibly in Ce6@CDC without laser irradiation. In contrast, the green fluorescence intensity in Ce6@CDC with laser irradiation and

Ce6-CPN@CDC without laser irradiation increased significantly, suggesting the generation of ROS. Moreover, the ROS production of Ce6-CPN@CDC with laser irradiation was significantly higher than that of other groups. This indicated that the combination of CDT and PDT may achieve the most effective therapeutic outcome. This was also supported by the quantitative analysis using flow cytometry (Fig. 3b and c).

3.4 Antitumor activity of Ce6-CPN@CDC *in vitro*

The cellular uptake process is a crucial factor in the anti-tumor activity of Ce6-CPN@CDC. Thus, MDA-MB-231 cells were incubated with Ce6-CPN@CDC for different durations and imaged using a confocal laser scanning microscope (CLSM). As presented in Fig. 4a and b, the red fluorescence intensity was not obvious in 1 h, indicating that only a small amount of nanoparticles entered the MDA-MB-231 cells. However, the red fluorescence increased gradually with prolonged incubation time (2–4 h), indicating efficient internalization of Ce6-CPN@CDC into MDA-MB-231 cells.

The tumor inhibitory effect of the nanoparticles was first studied in MDA-MB-231 cells using the MTT assay (Fig. 4c). After laser irradiation (denoted as “+L”), the anticancer effect of Ce6@CDC significantly enhanced as the concentration of Ce6 increased, which was caused by single PDT. Meanwhile, Ce6-CPN@CDC exhibited a significant inhibitory effect, which was attributed to the production of $\cdot\text{OH}$. Compared with the

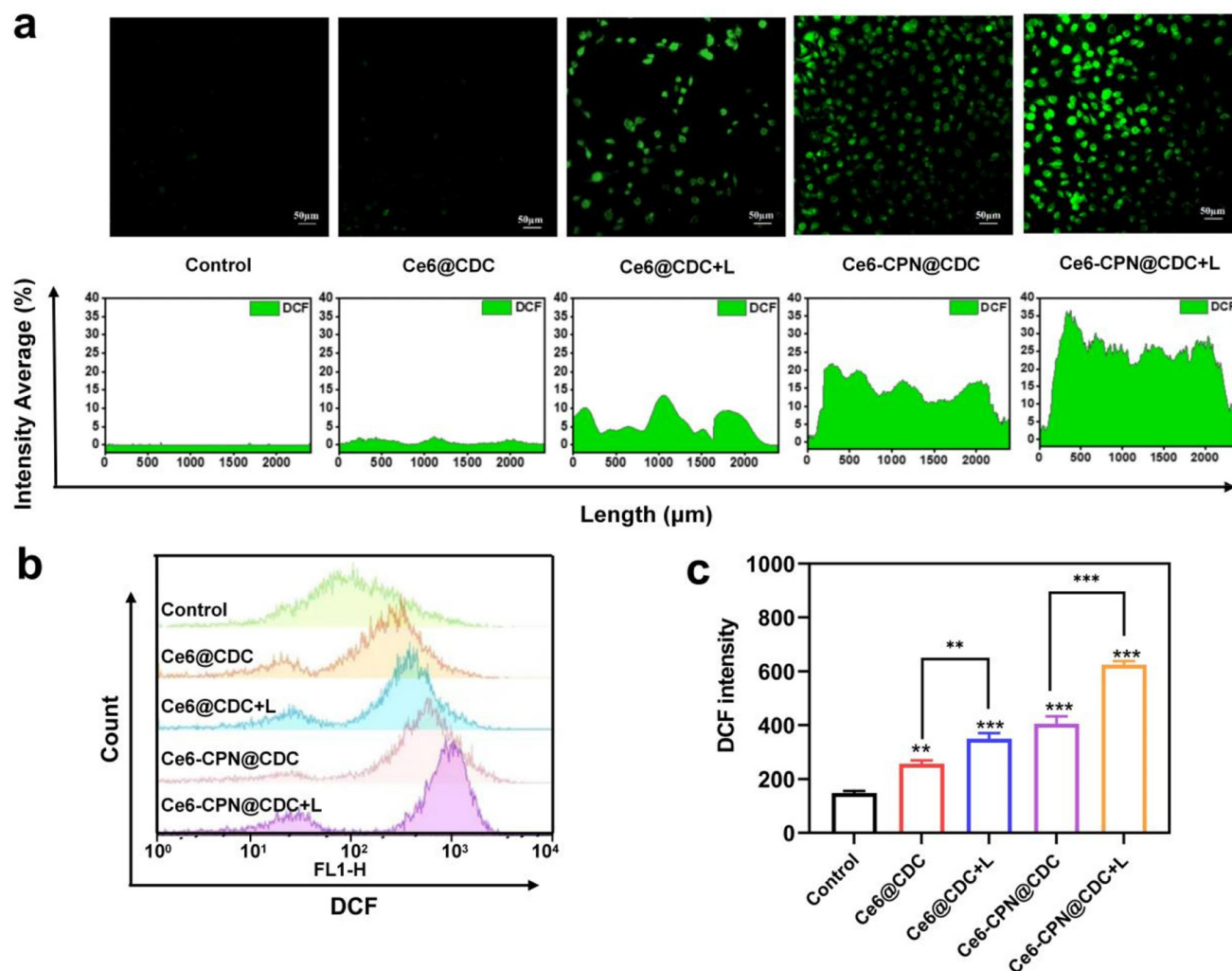


Fig. 3 (a) ROS level detection in MDA-MB-231 cells after incubation with PBS, Ce6@CDC and Ce6-CPN@CDC with or without laser irradiation for 4 h. (b and c) Flow cytometry analysis of ROS generation in MDA-MB-231 cells after various treatments. Scale bars: 50 μm. $n = 3$, $**P < 0.01$, moderately significant; $***P < 0.001$, highly significant.

other groups, the survival rate was the lowest in Ce6-CPN@CDC with laser irradiation, suggesting that the synergistic CDT/PDT could be achieved by Ce6-CPN@CDC.

To intuitively illustrate the anti-tumor activity of the nanoparticles, live/dead stained MDA-MB-231 cells were analyzed using calcein-AM/PI double staining. Notably, almost all MDA-MB-231 cells were killed after treatment with Ce6-CPN@CDC under laser irradiation (Fig. 4d), while MDA-MB-231 cells were only slightly damaged after treatment with Ce6-CPN@CDC without laser irradiation and Ce6@CDC with laser irradiation. Therefore, Ce6-CPN@CDC with laser irradiation could accomplish a satisfactory CDT and PDT effect *in vitro*.

Moreover, as presented in Fig. 4e, the apoptosis rate of MDA-MB-231 cells incubated with Ce6@CDC with laser irradiation was higher than that observed with Ce6@CDC, indicating that PDT occurred *via* Ce6. Moreover, the apoptosis rate in the Ce6-CPN@CDC with laser irradiation group signifi-

cantly increased to 32.6%, compared to those in the groups treated with Ce6@CDC with laser irradiation (14.88%) and Ce6-CPN@CDC without laser irradiation (16.09%), consistent with the above results. These data demonstrated that Ce6-CPN@CDC with laser irradiation could effectively induce apoptosis in MDA-MB-231 cells.

In addition, the ability of the nanoparticles to inhibit tumor cell invasion was also further investigated through wound healing experiments. Compared with the control, the wound was partly healed in Ce6@CDC with laser irradiation or Ce6-CPN@CDC without laser irradiation, while Ce6-CPN@CDC with laser irradiation had a negligible effect on the wound (Fig. S6, ESI†). Therefore, these results suggested that Ce6-CPN@CDC with laser irradiation had the ability to inhibit the invasion of tumor cells, achieving a synergistic anticancer effect. Based on the above results, Ce6-CPN@CDC holds promise as a synergistic tool in the combination of PDT and CDT.

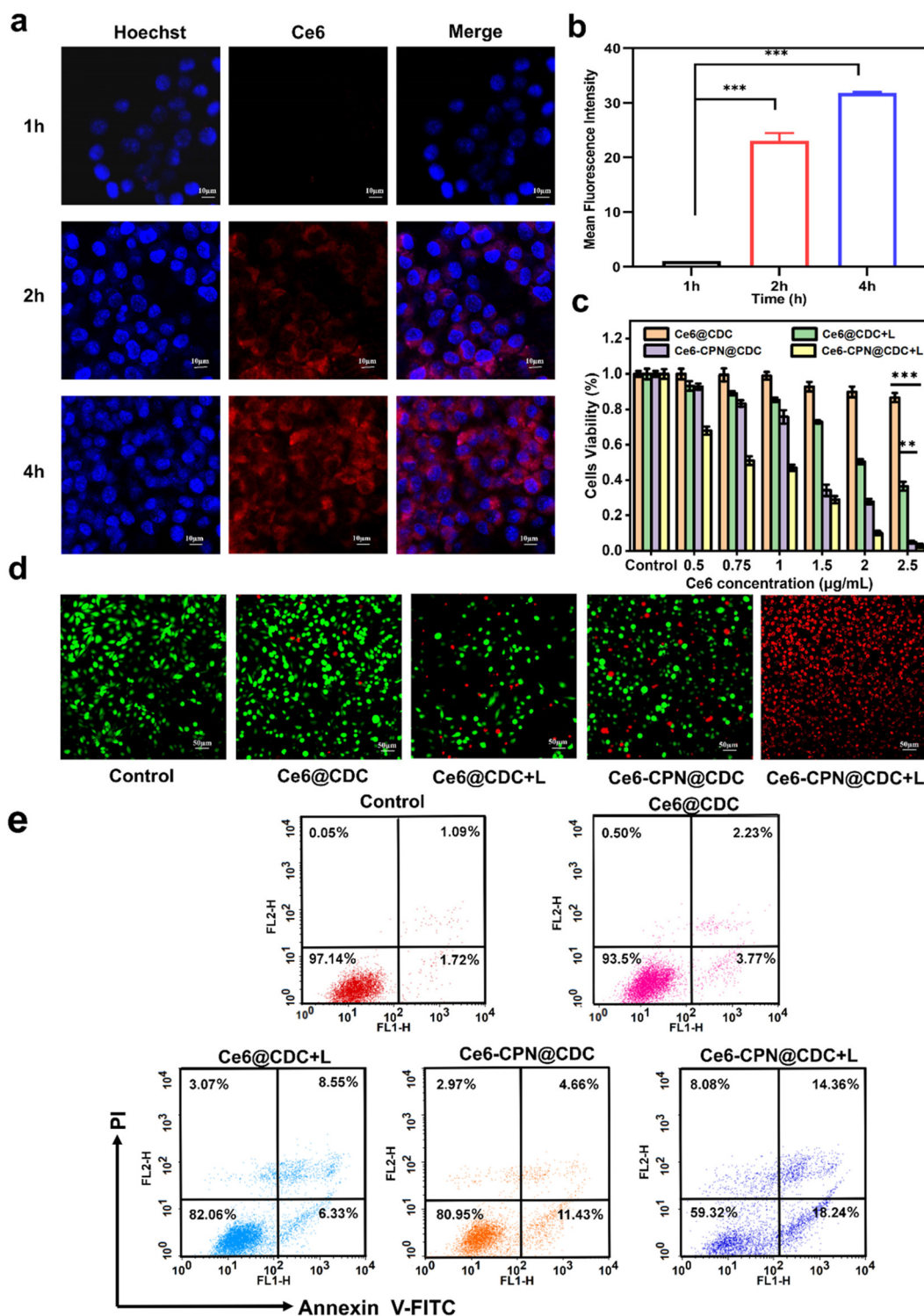


Fig. 4 (a) CLSM images of MDA-MB-231 cells treated with Ce6-CPN@CDC at different times. Blue fluorescence and red fluorescence represent Hoechst and Ce6, respectively. (b) Quantitative analysis of the mean fluorescence intensity (MFI) of (a). (c) Cell viability of MDA-MB-231 cells after treatment with Ce6@CDC and Ce6-CPN@CDC for 24 h with or without laser irradiation. (d) CLSM images of MDA-MB-231 cells pre-incubated with different nanoparticles, colabeled with calcein AM (green) and PI (red). (e) Cell apoptosis analysis. Mean \pm SD, $n = 3$, ** $P < 0.01$, moderately significant; *** $P < 0.001$, highly significant.

3.5 The evaluation of antitumor immune response

Numerous studies have shown that ICD-based immunotherapeutic strategies have great potential in cancer therapy. In the process of ICD, tumor-associated antigens and damage-associated molecular patterns (DAMPs) are exposed, involving the expression of cell-surface calreticulin (CRT) on the surface, as well as the enhanced release of high-mobility group box 1 (HMGB1) and adenosine triphosphate (ATP). Calreticulin (CRT), as an “eat me” signal, is transferred to the cell membrane and recognized by antigen-presenting cells (APCs, such as DCs), activating the cytotoxicity of T lymphocytes. As illustrated in Fig. 5a, the cells treated with Ce6@CDC showed weak CRT exposure, indicating a low ICD effect. The cells treated with Ce6@CDC with laser irradiation and Ce6-CPN@CDC without laser irradiation exhibited more CRT exposure. Notably, treatment with Ce6-CPN@CDC with laser irradiation led to the highest level of CRT exposure. Western blot analysis of CRT (Fig. 5b and Fig. S8b, ESI†) also confirmed this result. Moreover, the release of HMGB1 was evaluated by CLSM. The cells treated with Ce6-CPN@CDC with laser irradiation exhibited stronger red fluorescence representing HMGB1 (Fig. S7 and S8c, ESI†). Next, western blot was used for semi-quantitative evaluation of the HMGB1 protein, yielding results similar to those of CLSM (Fig. 5b and Fig. S8d, ESI†). Additionally, extracellular release of ATP can serve as a “find me” signal to enhance the activation of APCs. Thus, ATP was tested using an enzyme-linked immunosorbent assay (ELISA) (Fig. 5c). The ATP level in the cell supernatant of Ce6-CPN@CDC with laser irradiation increased 6.4-fold compared to the control group, while in the Ce6@CDC, Ce6@CDC with laser irradiation, and Ce6-CPN@CDC without laser irradiation groups, it was upregulated 6-, 3.4- and 2.6-fold, respectively. These above results demonstrated that the combined CDT and PDT undoubtedly exhibited a stronger ICD stimulus than single CDT or PDT, especially in Ce6-CPN@CDC with laser irradiation, which improved the antitumor efficacy.

As a DNA receptor, cyclic GMP-AMP synthase (cGAS) plays a crucial role in the immune system by recognizing abnormal DNA in the cytoplasm and activating the stimulator of interferon gene (STING) signaling pathway. This signaling cascade reaction leads to an immune response produced by type I interferon and other immune mediators (Fig. 5d). Since free dsDNA fragments released by nuclear damage play an important role in the activation of the cGAS-STING pathway^{35,36} we performed immunostaining of dsDNA in 231 cells using γ -H2AX, a specific indicator of cellular nuclear damage. As presented in Fig. 5e, compared to the barely visible red fluorescence signal in the PBS and Ce6@CDC groups, a more intense red signal was observed in the Ce6@CDC with laser irradiation group and the Ce6-CPN@CDC without laser irradiation group. The most pronounced red signal was detected in the Ce6-CPN@CDC with laser irradiation group, indicating that Ce6-CPN@CDC with laser irradiation had the ability to induce more DNA damage *via* the combination of PDT and CDT.

Then, cGAS was detected by immunofluorescence staining. As shown in Fig. 5j, a more intense red signal was captured in Ce6-

CPN@CDC with laser irradiation, revealing that the expression of cGAS significantly increased in Ce6-CPN@CDC with laser irradiation, leading to enhanced activation of the STING pathway. Afterwards, the protein expression levels of cGAS-STING-related markers including phosphorylated STING (p-STING), p-TBK1 and p-IRF3 were visualized by western blotting to assess the activation of the cGAS-STING pathway (Fig. 5f-i). The highest level of phosphorylated STING (p-STING as the golden standard) was observed in the Ce6-CPN@CDC with laser irradiation group, which was at least 4.1-, 3.2-, 2.1- and 1.9-fold higher compared to those in the other treated groups, respectively. Similarly, STING-dependent TBK1 and IRF3 phosphorylation as an indicator for STING activation in Ce6-CPN@CDC with laser irradiation was higher than that of the control group and other experimental groups, further indicating that Ce6-CPN@CDC with laser irradiation activated the cGAS-STING pathway.

The cyclic GMP-AMP synthase (cGAS)-STING pathway, as an endogenous mechanism of the innate immune system, can activate anti-tumor immune responses through the spontaneous secretion of type I interferon (IFN-I) and pro-inflammatory cytokines. Therefore, several immune-relevant cytokines were examined by ELISA to confirm the immune activation. In terms of IFN- β , a crucial downstream event of the STING signaling pathway, the Ce6-CPN@CDC with laser irradiation group resulted in a higher production compared to the control, CDT alone and PDT alone groups (Fig. 5k). Additionally, the same treatment showed a similar increase in the production of TNF- α , another pro-inflammatory cytokine (Fig. 5l). Similarly, the content of IL-6 in the serum exhibited the same trend in mice treated with Ce6-CPN@CDC with laser irradiation. The highest level of IL-6 was observed in the Ce6-CPN@CDC with laser irradiation group, which was at least 4-, 3.2-, 2.5- and 1.8-fold higher than those in the other treated groups, respectively (Fig. 5m). Thus, Ce6-CPN@CDC with laser irradiation could induce a higher level of immune response.

Both ICD induction and cGAS-STING pathway activation have been reported to lead to the maturation of dendritic cells (DCs).^{37–39} Subsequently, the mature DCs present antigens to cytotoxic T lymphocytes. Therefore, we evaluated the maturation of mouse bone marrow-derived dendritic cells (BMDCs) treated with nanoparticles *in vitro* and *in vivo*. The immunoassay of DC maturation was first performed. As a result, there was no difference in inducing DC maturation between Ce6@CDC and the control. However, treatment with Ce6-CPN@CDC with laser irradiation *in vitro* exhibited more DC maturation markers, CD80 and CD86, further proving the release of tumor-associated antigens induced by Ce6-CPN@CDC with laser irradiation (Fig. 5n). Again, CLSM revealed that the maturation of DCs in mice treated with Ce6-CPN@CDC with laser irradiation *in vivo* was significantly higher than that of the remaining groups, which was ascribed to the collective efforts of PDT- and CDT-induced ICD stimulation and STING signal activation (Fig. S9, ESI†). In a word, these results revealed the capability of Ce6-CPN@CDC with laser irradiation to induce ICD and activate the cGAS-STING pathway, thereby stimulating DC maturation.

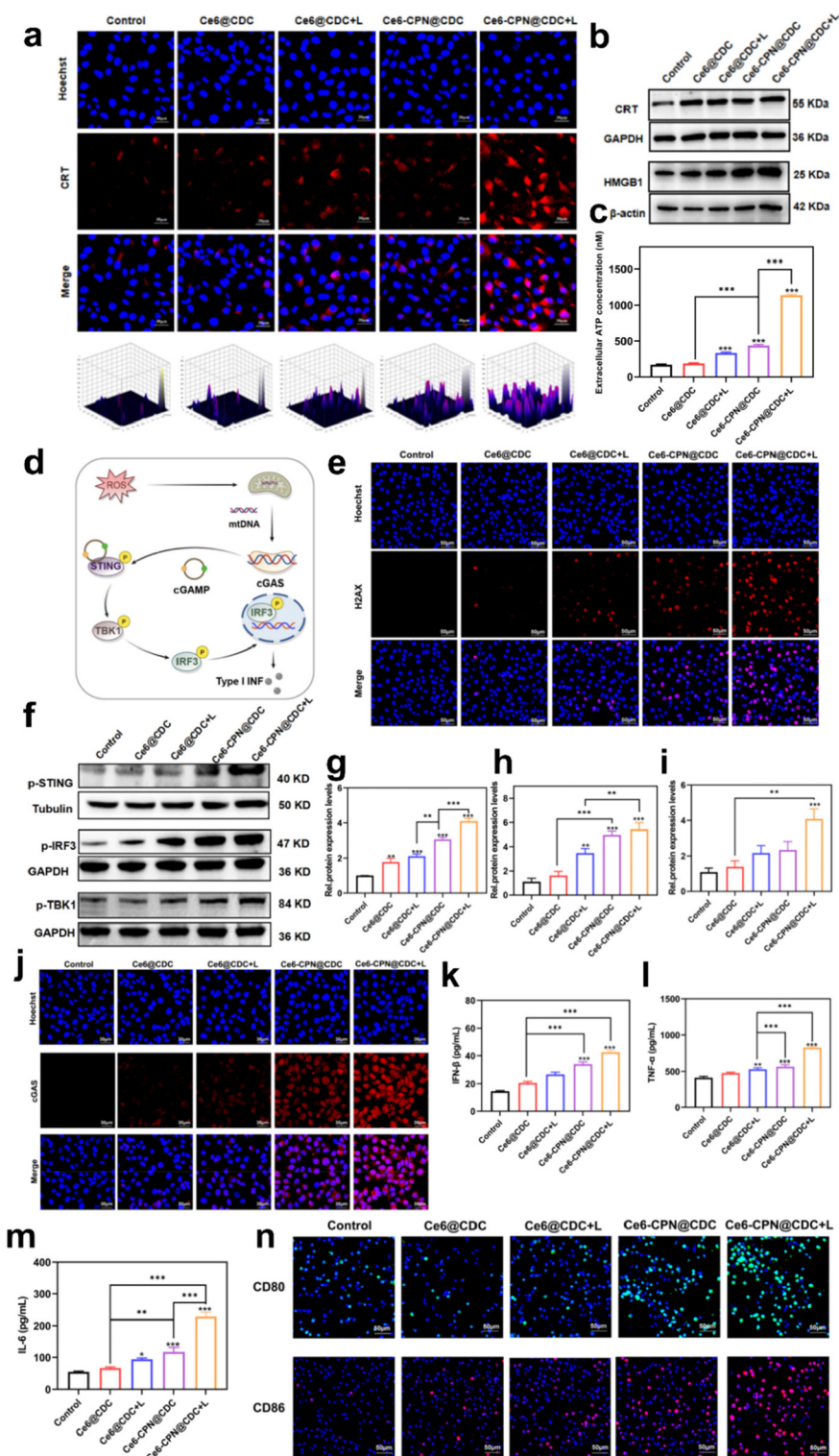


Fig. 5 (a) CLSM images of CRT expressed in MDA-MB-231 cells treated with different treatments. (b) Western blot analysis of CRT and HMGB1 expression. (c) ATP secretion from MDA-MB-231 cells after different treatments. (d) Schematic representation of cGAS-STING pathway activation. (e) Immunofluorescence images of γ H2AX expression in MDA-MB-231 cells treated with Ce6@CDC and Ce6-CPN@CDC with or without laser irradiation. (f) Western blot analysis on the expression of p-STING, p-IRF3 and p-TBK1 in MDA-MB-231 cells after 24 h of treatment. (g) Western blot quantification results of (f) p-STING in MDA-MB-231 cells after 24 h of treatment. (h) Western blot quantification results of (f) p-IRF3 in MDA-MB-231 cells after 24 h of treatment. (i) Western blot quantification results of (f) p-TBK1 in MDA-MB-231 cells after 24 h of treatment. (j) CLSM images of cGAS expressed in MDA-MB-231 cells after treatment with PBS, Ce6@CDC and Ce6-CPN@CDC with or without laser irradiation for 24 h. The levels of (k) interferon- β (IFN- β), (l) tumor necrosis factor- α (TNF- α) and (m) interleukin-6 (IL-6) released after different treatments. (n) Expression of CD80 and CD86 by BMDCs analyzed by CLSM. Scale bars: 50 μ m. $n = 3$, * $P < 0.05$, significant; ** $P < 0.01$, moderately significant; *** $P < 0.001$, highly significant.

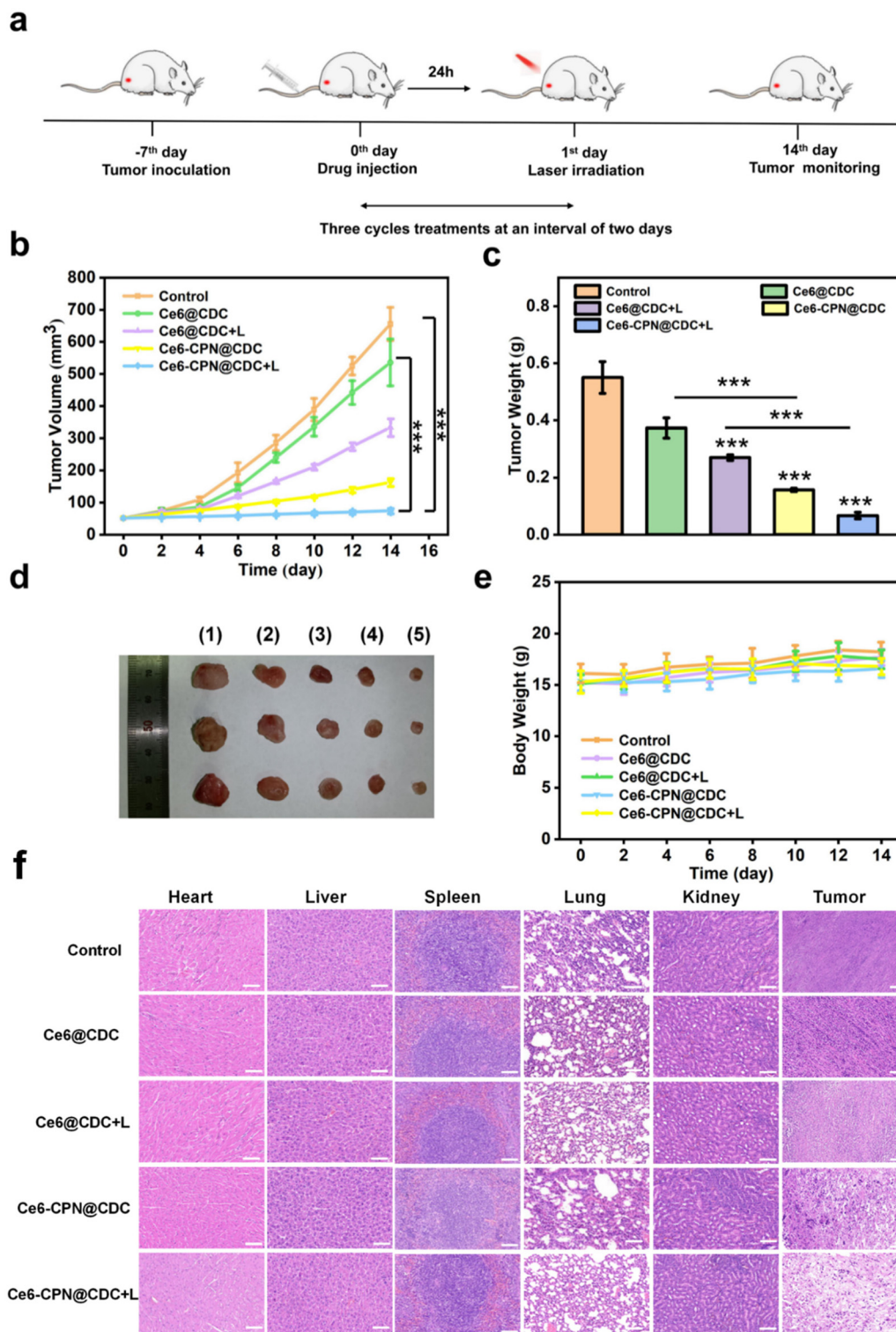


Fig. 6 (a) The schedule of TNBC treatment *in vivo*. (b) Tumor growth curves of the BALB/c mice with different treatments. (c) The tumor weight and (d) digital images for different groups on the 14th day of therapy. (e) Body weight of the mice during the therapy. (f) H&E staining of tissue sections from major organs and tumors of BALB/c mice in different groups. Scale bars: 100 μm . $n = 3$, * $P < 0.05$, significant; ** $P < 0.01$, moderately significant; *** $P < 0.001$, highly significant.

3.6 Biocompatibility and anti-tumor efficacy *in vivo*

Although nanoparticles were considered to effectively eliminate cancer cells, they may also increase the risk of cytotoxicity to normal tissue. Therefore, it was necessary to conduct biocompatibility experiments in this study. The biocompatibility of Ce6-CPN@CDC to normal cells was studied using 293T cells through wound healing experiments and MTT assays. As displayed in Fig. S10a and b,† the wound was nearly healed in all the treatment groups, and the cell viability was as high as 86% at a Ce6 concentration of $2.5 \mu\text{g mL}^{-1}$, indicating its good biocompatibility. Moreover, the hemolysis test suggested that Ce6@CDC and Ce6-CPN@CDC exhibited low hemolytic efficiency, which was also visually confirmed by the corresponding digital photographs (Fig. S10c, ESI†). In addition, no significant histopathological damage was noticed in the H&E staining of the major organs including the heart, liver, spleen, lungs, and kidneys, demonstrating good biosafety and potential use for further *in vivo* animal experiments (Fig. 6f).

The accumulation of Ce6-CPN@CDC at the tumor site is necessary for tumor suppression. Thus, the distribution of Ce6-CPN@CDC *in vivo* was confirmed by fluorescence imaging (Fig. S11a, ESI†). Ce6-CPN@CDC was injected through the caudal vein into 4T1 tumor-bearing BALB/c mice. The Ce6 fluorescence signals at the tumor site increased with time and reached the maximum at 24 h post-injection, indicating the significant accumulation of Ce6-CPN@CDC in tumor tissues. The mice were sacrificed and their major organs and tumors were collected for fluorescence imaging after tail vein injection for 48 h. As illustrated in Fig. S11b and c,† the targeted accumulation of Ce6-CPN@CDC in the liver and tumor was observed. These findings demonstrated the excellent tumor targeting ability and sustainability of Ce6-CPN@CDC, thereby resulting in precise tumor inhibition.

To evaluate the anti-tumor effects of these nanoparticles *in vivo*, we further investigated their efficacy in BALB/c mice bearing 4T1 cells (Fig. 6a). When the tumor volumes reached 50 mm^3 , the mice were divided into 5 groups randomly: (1) saline (control), (2) Ce6@CDC, (3) Ce6@CDC with laser irradiation, (4) Ce6-CPN@CDC and (5) Ce6-CPN@CDC with laser irradiation. As presented in Fig. 6b, the tumor volume in the Ce6@CDC group was uncontrolled, while the Ce6@CDC with laser irradiation group exhibited a slower tumor growth rate compared with the control group, confirming the efficiency of PDT. In addition, the tumor treated with Ce6-CPN@CDC without laser irradiation showed discernible tumor ablation, which was ascribed to CDT. More importantly, the mice receiving Ce6-CPN@CDC with laser irradiation showed the best tumor inhibition, suggesting the synergistic effects of CDT/PDT and immunotherapy. In addition, the tumor weight of the Ce6-CPN@CDC with laser irradiation treated mice was significantly smaller than those of the control as well as CDT alone and PDT alone groups (Fig. 6c). Moreover, digital tumor images from each group were also taken. The photographs of the tumors from each group directly demonstrated the superior therapeutic effect of Ce6-CPN@CDC with laser

irradiation (Fig. 6d). Furthermore, the body weight changes of each tumor-bearing mouse did not fluctuate significantly, further suggesting no severe toxic side effects of these nanoparticles (Fig. 6e). To further evaluate therapeutic efficacy, H&E staining of tumors collected from different groups was carried out. As shown in Fig. 6f, tumor tissues in the Ce6@CDC group exhibited thriving tumor cells with minor damage in comparison with the control group. Partial tissue destruction and a reduction in highly active tumor cells were observed in the Ce6@CDC with laser irradiation group and the Ce6-CPN@CDC without laser irradiation group, indicating a certain degree of necrosis of the tumors. The Ce6-CPN@CDC with laser irradiation group, however, showed significant tissue loss, nuclear shrinkage and pyknosis in the tumor. Based on the above results, Ce6-CPN@CDC with laser irradiation demonstrated effective tumor inhibition and good biocompatibility.

4. Conclusions

In this study, a pH- and GSH-responsive nanoparticle Ce6-CPN@CDC was constructed for PDT/CDT synergistic treatments to improve anti-tumor effects and activate immunotherapy. Upon endocytosis by cancer cells, CPN components could release Cu^{2+} and H_2O_2 under the acidic tumor conditions, producing highly toxic $\cdot\text{OH}$ via a Cu-based Fenton-like reaction, thereby achieving efficient CDT. Meanwhile, a large amount of singlet oxygen ($^1\text{O}_2$) could be generated from the released Ce6 within a short period, exerting a robust photodynamic anti-cancer effect. Moreover, the ROS production led to DNA damage in tumor cells and activated the cGAS-STING pathway, thereby stimulating a systemic anti-tumor immune response. The activated cGAS-STING pathway further enhanced the production of type I interferons and the secretion of pro-inflammatory cytokines (such as $\text{TNF-}\alpha$ and IL-6), promoting immune cell infiltration and activating cytotoxic T cells to eliminate cancer cells. At the same time, this nanoparticle could further induce immunogenic cell death (ICD), leading to the release of DAMPs that triggered a robust antitumor immune response. Overall, we proposed a safe and efficient approach for cancer treatment that integrated photodynamic therapy, chemodynamic therapy and immunotherapy. This strategy could markedly inhibit the growth of TNBC and hold significant promise as a new approach in anti-cancer therapy.

Data availability

The data that support the findings of this study are available from the corresponding author upon reasonable request.

Conflicts of interest

The authors declare that they have no known competing financial interests or personal relationships that could have appeared to influence the work reported in this paper.

Acknowledgements

We acknowledge the support of the Hebei North University Foundation (8237120930 and B2022405004) and the PhD Start-Up Fund of Hebei North University (BSJJ202307).

References

- X. Sun, Y. Zhang, J. Li, K. S. Park, K. Han, X. Zhou, Y. Xu, J. Nam, J. Xu, X. Shi, L. Wei, Y. L. Lei and J. J. Moon, *Nat. Nanotechnol.*, 2021, **16**, 1260–1270.
- J. Wang, P. Li, Y. Yu, Y. Fu, H. Jiang, M. Lu, Z. Sun, S. Jiang, L. Lu and M. X. Wu, *Science*, 2020, **367**, eaau0810.
- P. N. Kelly, *Science*, 2018, **359**, 1344–1345.
- Q. Zhou, D. Dutta, Y. Cao and Z. Ge, *ACS Nano*, 2023, **17**, 9374–9387.
- B. Feng, F. Zhou, B. Hou, D. Wang, T. Wang, Y. Fu, Y. Ma, H. Yu and Y. Li, *Adv. Mater.*, 2018, **30**, e1803001.
- B. J. Wadsworth, R. A. Cederberg, C. M. Lee, N. S. Firmino, S. E. Franks, J. Pan, N. Colpo, K. S. Lin, F. Benard and K. L. Bennewith, *Cancer Lett.*, 2020, **493**, 31–40.
- K. Hu, L. Miao, T. J. Goodwin, J. Li, Q. Liu and L. Huang, *ACS Nano*, 2017, **11**, 4916–4925.
- B. Wang, Q. Zhao, Y. Zhang, Z. Liu, Z. Zheng, S. Liu, L. Meng, Y. Xin and X. Jiang, *J. Exp. Clin. Cancer Res.*, 2021, **40**, 24.
- Z. Chen, Z. Li, H. Huang, G. Shen, Y. Ren, X. Mao, L. Wang, Z. Li, W. Wang, G. Li, B. Zhao, W. Guo and Y. Hu, *Small*, 2023, **19**, e2302758.
- J. I. Jiménez-Loygorri, B. Villarejo-Zori, Á. Viedma-Poyatos, J. Zapata-Muñoz, R. Benítez-Fernández, M. D. Frutos-Lisón, F. A. Tomás-Barberán, J. C. Espín, E. Area-Gómez, A. Gomez-Duran and P. Boya, *Nat. Commun.*, 2024, **15**, 830.
- H. Lv, Q. Zong, C. Chen, G. Lv, W. Xiang, F. Xing, G. Jiang, B. Yan, X. Sun, Y. Ma, L. Wang, Z. Wu, X. Cui, H. Wang and W. Yang, *Nat. Commun.*, 2024, **15**, 6.
- R. Wang, A. Hussain, Q. Guo and M. Ma, *Crit. Rev. Oncol. Hematol.*, 2024, **193**, 104194.
- Z. Gu, Y. Hao, T. Schomann, F. Ossendorp, P. ten Dijke and L. J. Cruz, *J. Controlled Release*, 2023, **357**, 531–544.
- J. Zheng, J. Mo, T. Zhu, W. Zhuo, Y. Yi, S. Hu, J. Yin, W. Zhang, H. Zhou and Z. Liu, *Mol. Cancer*, 2020, **19**, 133.
- M. Jiang, P. Chen, L. Wang, W. Li, B. Chen, Y. Liu, H. Wang, S. Zhao, L. Ye, Y. He and C. Zhou, *J. Hematol. Oncol.*, 2020, **13**, 81.
- Q. Liu, J. Tian, Y. Tian, Q. Sun, D. Sun, F. Wang, H. Xu, G. Ying, J. Wang, A. K. Yetisen and N. Jiang, *ACS Nano*, 2021, **15**, 515–525.
- Q. Xie, Z. Li, Y. Liu, D. Zhang, M. Su, H. Niitsu, Y. Lu, R. J. Coffey and M. Bai, *Acta Biomater.*, 2021, **134**, 716–729.
- W. Yang, F. Zhang, H. Deng, L. Lin, S. Wang, F. Kang, G. Yu, J. Lau, R. Tian, M. Zhang, Z. Wang, L. He, Y. Ma, G. Niu, S. Hu and X. Chen, *ACS Nano*, 2020, **14**, 620–631.
- T. Li, Y. Zhang, J. Zhu, F. Zhang, A. Xu, T. Zhou, Y. Li, M. Liu, H. Ke, T. Yang, Y. Tang, J. Tao, L. Miao, Y. Deng and H. Chen, *Adv. Mater.*, 2023, **35**, e2210201.
- L. Li, H. Tian, Z. Zhang, N. Ding, K. He, S. Lu, R. Liu, P. Wu, Y. Wang, B. He, M. Luo, P. Peng, M. Yang, E. C. Nice, C. Huang, N. Xie, D. Wang and W. Gao, *ACS Appl. Mater. Interfaces*, 2022, **15**, 452–468.
- Z. Liu, Z. Xie, W. Li, X. Wu, X. Jiang, G. Li, L. Cao, D. Zhang, Q. Wang, P. Xue and H. Zhang, *J. Nanobiotechnol.*, 2021, **19**, 160.
- L. Chen, S. Yan, W. J. Guo, L. Qiao, X. Zhan, B. Liu and H. Q. Peng, *Chem. Sci.*, 2024, **15**, 16059–16068.
- S. Wang, Q. Wang, Y. Lv, Z. Liu, K. Lee, D. Kim, M. Won, J. Shen and J. S. Kim, *Aggregate*, 2025, **6**, e737.
- J. Xu, L. Xu, C. Wang, R. Yang, Q. Zhuang, X. Han, Z. Dong, W. Zhu, R. Peng and Z. Liu, *ACS Nano*, 2017, **11**, 4463–4474.
- J. Dang, H. He, D. Chen and L. Yin, *Biomater. Sci.*, 2017, **5**, 1500–1511.
- L. Zhang, C. X. Li, S. S. Wan and X. Z. Zhang, *Adv. Healthcare Mater.*, 2022, **11**, e2101971.
- C. Yang, H. Ou, L. Mo and W. Lin, *J. Mater. Chem. B*, 2023, **11**, 11310–11318.
- F. Liu, T. He, S. Gong, M. Shen, S. Ma, X. Huang, L. Li, L. Wang, Q. Wu and C. Gong, *Acta Biomater.*, 2022, **154**, 510–522.
- X. Cao, S. Li, W. Chen, H. Lu, L. Ye, Z. Min, S. Sun, C. Teng, H. Yin, Q. Zhang, W. He, X. Wang, W. Lv, L. Lv and H. Xin, *ACS Appl. Mater. Interfaces*, 2022, **14**, 27623–27633.
- J. Wang, J. Si, J. Li, P. Zhang, Y. Wang, W. Zhang, B. Jin, W. Li, N. Li and S. Miao, *ACS Appl. Mater. Interfaces*, 2021, **13**, 49017–49026.
- S. Fu, M. Wang, B. Li, X. Li, J. Cheng, H. Zhao, H. Zhang, A. Dong, W. Lu and X. Yang, *Biomater. Res.*, 2023, **27**, 43.
- G. Li, Y. Bao, H. Zhang, J. Wang, X. Wu, R. Yan, Z. Wang and Y. Jin, *J. Colloid Interface Sci.*, 2024, **668**, 618–633.
- Z. Zhou, H. Liang, R. Yang, Y. Yang, J. Dong, Y. Di and M. Sun, *Angew. Chem., Int. Ed.*, 2022, **61**, e202202843.
- L. H. Fu, Y. Wan, C. Qi, J. He, C. Li, C. Yang, H. Xu, J. Lin and P. Huang, *Adv. Mater.*, 2021, **33**, e2006892.
- H. Tian, N. Zhu, H. Wang, Y. Li, Q. Yang, H. Chen, Z. Zhou, J. Tan, H. Zheng, J. Xie, W. Li, M. Liang, Z. Guo and Z. Li, *Small*, 2024, **20**, e2403428.
- X. Zhao, K. Zhang, Y. Wang, W. Jiang, H. Cheng, Q. Wang, T. Xiang, Z. Zhang, J. Liu and J. Shi, *Adv. Funct. Mater.*, 2022, **32**, 2108883.
- L. Ding, Q. Wang, A. Martincuks, M. J. Kearns, T. Jiang, Z. Lin, X. Cheng, C. Qian, S. Xie, H. J. Kim, I. M. Launonen, A. Färkkilä, T. M. Roberts, G. J. Freeman, J. F. Liu, P. A. Konstantinopoulos, U. Matulonis, H. Yu and J. J. Zhao, *J. Immunother. Cancer*, 2023, **11**, e005627.
- L. Wang-Bishop, M. Wehbe, D. Shae, J. James, B. C. Hacker, K. Garland, P. P. Chistov, M. Rafat, J. M. Balko and J. T. Wilson, *J. Immunother. Cancer*, 2020, **8**, e000282.
- Y. Guo, R. Qian, Z. Li, T. Lv, C. Yang, W. Li, T. Pan, X. Hou and Z. Wang, *Life Sci.*, 2024, **348**, 122687.